Received: 8 March 2023 | Revised: 27 October 2023 | Accepted: 30 October 2023

DOI: 10.1002/mrm.29927

TECHNICAL NOTE

Magnetic Resonance in Medicine

Model-based reconstruction for looping-star MRI

Haowei Xiang[1] | **Jeffrey A. Fessler**[1,2] | **Douglas C. Noll**[2]

[1]EECS, University of Michigan, Ann Arbor, Michigan, USA

[2]Biomedical Engineering, University of Michigan, Ann Arbor, Michigan, USA

Correspondence
Haowei Xiang, EECS, University of Michigan, 1301 Beal Ave, Ann Arbor, MI 48109, USA.
Email: haoweix@umich.edu

Funding information
National Institutes of Health, Grant/Award Number: R01 EB023618

Abstract

Purpose: The aim of this study was to develop a reconstruction method that more fully models the signals and reconstructs gradient echo (GRE) images without sacrificing the signal to noise ratio and spatial resolution, compared to conventional gridding and model-based image reconstruction method.

Methods: By modeling the trajectories for every spoke and simplifying the scenario to only echo-in and echo-out mixture, the approach explicitly models the overlapping echoes. After modeling the overlapping echoes with two system matrices, we use the conjugate gradient algorithm (CG-SENSE) with the nonuniform FFT (NUFFT) to optimize the image reconstruction cost function.

Results: The proposed method is demonstrated in phantoms and in-vivo volunteer experiments for three-dimensional, high-resolution T2*-weighted imaging and functional MRI tasks. Compared to the gridding method, the high resolution protocol exhibits improved spatial resolution and reduced signal loss as a result of less intra-voxel dephasing. The fMRI task shows that the proposed model-based method produced images with reduced artifacts and blurring as well as more stable and prominent time courses.

Conclusion: The proposed model-based reconstruction results shows improved spatial resolution and reduced artifacts. The fMRI task shows improved time series and activation map due to the reduced overlapping echoes and under-sampling artifacts.

KEYWORDS

model-based reconstruction, silent MRI, ZTE

1 | INTRODUCTION

Functional MRI (fMRI) has evolved into the dominant tool for noninvasive imaging of human brain activity. However, the loud acoustic noise in MRI still remains a problem. For example, acoustic noise can cause discomfort and anxiety in patients,[1] especially for certain groups of individuals like children or patients with dementia. Furthermore, acoustic noise is an additional confounding sensory stimulus,[2-4] and can impact the blood-oxygen level dependent (BOLD) response as a function of both its loudness[5] and duration.[6] There are several ways[7] that acoustic noise can impact fMRI tasks and degrade measured task signals. First, acoustic noise from the scanner stimulates the auditory pathway (including the auditory cortex), reducing sensitivity to experimental stimuli.[8] Second, successfully processing degraded stimuli may require additional executive processes[9] (such as verbal working

memory or performance monitoring). Finally, scanner noise may cause participant discomfort and increase attentional demands, even for nonauditory tasks.

Although there are many sources of acoustic noise such as gradient coils, radiofrequency (RF) pulses, cryogenic pumps, and air circulating systems, the main acoustic noise comes from Lorentz forces caused by rapidly changing currents in the magnetic field gradient coils used primarily for spatial localization.[10] Acoustic noise levels can be reduced by hardware modifications, such as gradient designs and shielding,[11] quiet scanning mode provided by the vendors,[12] and pulse sequence design.[13]

Looping-star[14] is a silent MRI pulse sequence that has been used for quantitative susceptibility mapping, T2*-weighted imaging and fMRI.[15] It uses multiple RF pulses and slowly varying gradients so the acoustic noise is greatly reduced compared to the standard EPI method. This property makes it well suited for cases where low acoustic noise is required, such as pediatric MRI[16] and auditory fMRI tasks.[17] On the other hand, using multiple RF pulses with repeating slowly varying gradients can complicate k-space trajectories and make the reconstruction problem harder. The problem that leads to the most artifact is called the overlapping-echo effect, caused by signals from multiple excitation pulses being simultaneously present while looping through k-space locations.

Multiple methods have been proposed to reduce the overlapping echo artifacts. The first method[14] assumes that the echo-out and echo-in signal dominates the acquired signal at the beginning and the end of the sampling period, thus separating the overlapping echoes at the cost of lower signal-to-noise-ratio (SNR) and spatial resolution. The second method, RF-phase cycling, requires an additional scan with π RF phase change and then separates the overlapping echoes by doing a linear combination of signals from these two scans. This method can increase the SNR by a $\sqrt{2}$ at the cost of doubled scan time. The third method,[18] coherence-resolved looping-star, uses half as many RF pulses with increased time intervals to separate the echoes. It can be viewed as the same as the standard windowing method, but starting with fewer spokes and a higher resolution input. This method has half as many spokes as the original looping star, so it needs a longer scan time for structural MRI and has worse temporal resolution in fMRI tasks when matching the overall undersampling factor. None of the previous methods can separate the overlapping echoes without sacrificing scan time, spatial resolution, or SNR. In this paper, we propose a model-based reconstruction approach[19] that can theoretically resolve the overlapping echoes and maintain the resolution without increasing the scan time, building on our preliminary work in Reference 20. Along with the model-based reconstruction method, we used three-dimensional (3D) golden-angle-based k-space trajectories[21,22] for more uniform k-space coverage and reduced under-sampling artifacts.

There are a few reasons to expect that model-based reconstruction can perform better in looping-star MRI. First, the model-based reconstruction method uses more high-frequency data that is filtered out in the gridding reconstruction. Therefore, the image spatial resolution is improved, which can reduce signal loss in T2*-weighted imaging. Secondly, by modeling both echo-in and echo-out signals, the overlapping echoes are mostly resolved, whereas the gridding method neglects either the echo-in or echo-out signal. Thirdly, model-based reconstruction naturally uses the sensitivity maps for SENSE parallel imaging reconstruction,[23] reducing undersampling artifacts. Lastly, applying an appropriate regularizer can reduce image noise and improve image quality.

2 | METHODS

2.1 | Looping-star physical parameters

The looping-star sequence was developed to acquire T_2^*-weighted gradient-echo imaging data while maintaining its quiet performance. We used TOPPE[24] to separately generate excitation and acquisition modules and then combined those modules to form the pulse sequence. Our implementation can be easily extended to other variants of looping star by editing or adding modules. Figure 1 illustrates the pulse sequence diagram for looping-star fMRI and the corresponding k-space trajectory. During the first half of the sequence, the radial spokes are excited using a burst of short hard RF pulses[25] with a slowly changing gradient to control the direction of the trajectory. During this part, one can acquire a free-induction-decay (FID) image at echo time (TE) $\approx$ 0, though we did not use the FID data for the current work. The second half of the sequence applies the same gradient again but without RF pulses to create the gradient echo (GRE) signal used to produce a GRE image at TE = 27.67 ms, which is expected to give sufficient functional BOLD contrast at 3T. Each RF subpulse produces a low-frequency line thorough the center of k-space; the collection encodes a disk in 3D k-space, and this gradient encoding can be repeated additional times for multiple GRE echoes. We generate the full 3D trajectory by rotating the two-dimensional (2D) k-space trajectories.

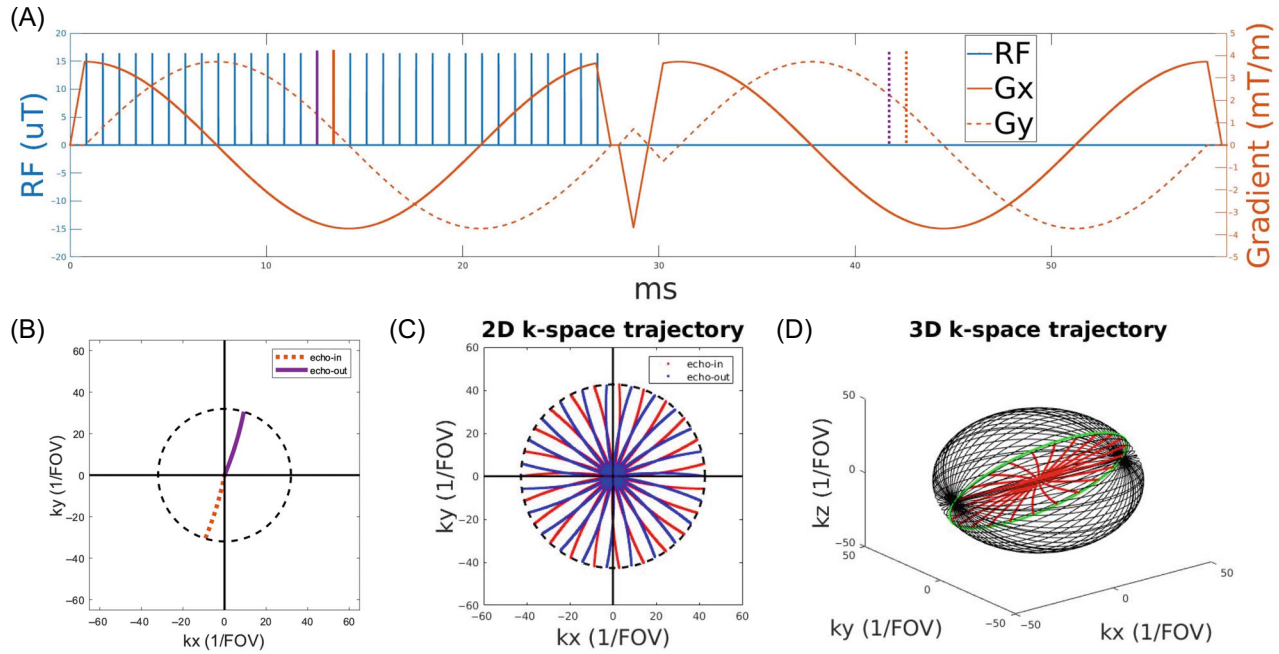

FIGURE 1 (A) A pulse sequence for a two-dimensional (2D) plane of the three-dimensional (3D) acquisition with one excitation/free-induction-decay (FID) module and one gradient echo (GRE)/data acquisition module (ramp-up and ramp-down gradient are required by TOPPE), the max slew rate for all modules (including ramps) is 5 mT/m/ms; (B) Illustration of overlapping echoes in GRE module: the echo-out signal from purple radiofrequency (RF) pulse overlaps the echo-in signal from orange RF pulse in time; (C) 2D GRE k-space trajectory: an odd number of spokes generates more evenly distributed spokes; (D) 3D k-space trajectory using 3D generalized golden-angle.

2.2 | Acquisition method

We designed several protocols for different needs including a hi-res protocol for structural imaging, and mid-res and low-res protocols for fMRI studies.

For structural imaging, we use 12 RF pulses with 2.24 ms readout per RF pulse to achieve about 1.25 mm isotropic resolution, which we call the high-resolution protocol. Two GRE echoes are collected to acquire images with TE = 27.67 ms and TE = 54.55 ms. For multiple GRE echoes, we define a separate forward model for each echo and reconstruct each echo independently. For fMRI studies, we designed two protocols with different spatial and temporal resolution. We found that an odd number of RF pulses produced more uniform 2D k-space coverage in the highly undersampled fMRI cases, so we used 23 RF pulses with 1.12 ms readout per RF pulse in mid-res protocol to achieve 3-mm isotropic spatial resolution and 3.6s temporal resolution, and 31 RF pulses with 0.84ms readout per RF pulse for low-resolution protocol to achieve 3.75-mm isotropic spatial resolution and 1.8-s temporal resolution. The RF pulse interval and gradient waveforms were adjusted such that the echo time is approximately 27.67 ms for both protocols. To produce an excitation profile that is as uniform as possible, we used a series of very short 12 μs RF pulses with near maximum magnitude in the excitation module with a flip angle of 3°.

For all protocols, we first designed a 2D sinusoidal gradient with acquisition dwell time of 4 μs, a maximum gradient amplitude of 5 mT/m and maximum slew rate of 1 mT/m/ms in terms of the root sum of square of x and y axes. Then in 3D, to achieve more uniform k-space spokes, we adopted the 3D golden-angle-based rotation[26] by generating a series of azimuth and polar angles with small increment. The 2D k-space trajectories were rotated along x axis by the azimuth angle and along the z axis by polar angle. We used 4800 3D rotations in hi-res protocol, 64 and 32 3D rotations for each time frame in mid-res and low-res fMRI protocols, respectively. The structural and fMRI protocols are tested in phantom and in vivo studies.

Because TOPPE currently requires the gradient of each module to start and end at zero, we used ramp-up and ramp-down gradients before and after the excitation and acquisition module to accommodate this constraint. The max slew rate of the ramp up and ramp down gradient was set to 5 mT/m/ms.

Sensitivity maps were estimated from a 2-min 3D GRE pulse sequence with 3-mm isotropic spatial resolution.

2.3 | Signal models in looping-star

In model-based reconstruction,[19] we approximate the object magnetization $f(\vec{r})$using a finite series

expansion as follows

$$f(\vec{r}) = \sum_{n=0}^{N-1} f_n \, b(\vec{r} - \vec{r}_n), \tag{1}$$

where $b(\cdot)$ denotes the object basis function, typically a voxel indicator function, $\vec{r}_n$ denotes the center of nth translated basis function, and N is the number of parameters (voxels).

In looping-star fMRI, assuming we have N_{rf} RF pulses in one cycle of FID and following GRE, there will be up to N_{rf} k-space trajectories, each corresponding to a previously applied RF pulse. Therefore, the GRE signal sampled at any time t is a superposition of N_{rf} k-space samples located on corresponding trajectories.

The corresponding signal equation for the ith spoke ($i = 1, \ldots, N_{\text{rf}}$) and jth receiver coil ($j = 1, \ldots, J$) is given by[19]

$$s_{ij}(t) = \int c_j(\vec{r}) f(\vec{r}) \left(\sum_{l=1}^{N_{\text{rf}}} \mathrm{e}^{-z(\vec{r})(t+(i-l)\Delta t)} \, \mathrm{e}^{-\imath 2\pi \vec{k}_l(t+(i-l)\Delta t)\cdot\vec{r}} \right) d\vec{r}, \tag{2}$$

where a continuous time index t is the time for the ith spoke starting from the end of the ith RF pulse, $c_j(\vec{r})$ is the sensitivity map of jth receiver coil, $f(\vec{r})$ is the unknown continuous complex transverse magnetization, $z(\vec{r}) \triangleq 1/T_2^*(\vec{r}) + \imath\Delta\omega_0(\vec{r})$ is the "rate map," Δt is the time interval between adjacent RF pulses, $(i-l)\Delta t$ is the time between the ith and lth RF pulse, and $\vec{k}_l(t)$ is the k-space trajectory for the lth RF pulse at time t.

Each l represents a RF pulse that contributes to the signal. When $l = i$, the corresponding k-space trajectory $\vec{k}_i(t)$ moves from the center k-space to outer k-space, which is called echo-out trajectory, and when $l = i+1$, the corresponding k-space trajectory $\vec{k}_{i+1}(t - \Delta t)$ moves from the outer k-space to center k-space, which is called echo-in trajectory.

After space discretization[27] using (1), we approximate (2) by

$$s_{ij}(t) = \sum_{l=1}^{N_{\text{rf}}} B(\vec{k}_l(t + (i-l)\Delta t)) \sum_{n=0}^{N-1} c_j(\vec{r}_n) f(\vec{r}_n) \, \mathrm{e}^{-z(\vec{r}_n)(t+(i-l)\Delta t)} \, \mathrm{e}^{-\imath 2\pi \vec{k}_l(t+(i-l)\Delta t)\cdot\vec{r}_n}, \tag{3}$$

where $B(\vec{k}(\cdot))$ denotes the spectrum of the object basis function $b(\cdot)$.

We express the noisy measured signals for ith spoke and jth coil in matrix-vector form as follows

$$\boldsymbol{s}_{ij} = \left(\sum_{l=1}^{N_{\text{rf}}} \boldsymbol{A}_{il} \right) \boldsymbol{C}_j \boldsymbol{f} + \boldsymbol{\epsilon}_{ij} \in \mathbb{C}^M, \tag{4}$$

where $\boldsymbol{f} = (f_1, \ldots, f_N)$ is the vector of parameters (voxel values) we hope to estimate from the measurement $\boldsymbol{s}$, $\boldsymbol{C}_j \in \mathbb{C}^{N\times N}$ is the diagonal sensitivity map matrix, and each element of the matrix $\boldsymbol{A}_{il} \in \mathbb{C}^{M\times N}$ is given by

$$a_{ilmn} = B(\vec{k}_l(t_m + (i-l)\Delta t)) \, \mathrm{e}^{-z(\vec{r}_n)(t_m+(i-l)\Delta t)} \, \mathrm{e}^{-\imath 2\pi \vec{k}_l(t_m+(i-l)\Delta t)\cdot\vec{r}_n}, \tag{5}$$

where i is the spoke index, j is the coil index, l is the RF pulse index, m is the index for a discrete time point in k-space, and n is the index for discrete image grid.

Stacking up all J measurement vectors and sensitivity map matrices from all coils and defining the system matrix for the ith echo to be $\boldsymbol{A}_i = \sum_{l=1}^{N_{\text{rf}}} \boldsymbol{A}_{il} \in \mathbb{C}^{M\times N}$ yields the linear model

$$\boldsymbol{s}_i = (\boldsymbol{I}_J \otimes \boldsymbol{A}_i) \, \boldsymbol{C}\boldsymbol{f} + \boldsymbol{\epsilon}_i, \tag{6}$$

where M is the number of samples per spoke, $\boldsymbol{C} = [\boldsymbol{C}_1; \ldots; \boldsymbol{C}_J] \in \mathbb{C}^{(JN)\times N}$, $\boldsymbol{I}_J$ is a $J \times J$ identity matrix, and $\otimes$ denotes the Kronecker product.

To perfectly model all the spokes, the optimal signal model would take all those k-space locations into account. However, modeling all the spokes would require approximately 512 cubic spatial resolution and in practice is computationally infeasible, especially in fMRI scans with many time frames. Our implementation simplifies the signal model to include only signals from echo-in spokes and echo-out spokes. Specifically, we simplify (6) to

$$\boldsymbol{s}_i = (\boldsymbol{I}_J \otimes \tilde{\boldsymbol{A}}_i) \, \boldsymbol{C}\boldsymbol{f} + \boldsymbol{\epsilon}_i, \tag{7}$$

where we use the two-term approximation $\tilde{\boldsymbol{A}}_i = \sum_{l\in\{i,i+1\}} \boldsymbol{A}_{il}$. Here $l = i+1$ corresponds to the echo-in spoke and $l = i$ corresponds to the echo-out spoke.

Two special cases are the first and last spokes, where an FID overlaps with a first GRE or an recalled GRE overlaps with a later gradient recalled echo, which are problematic due to the unknown T_2^* map and disparate signal strengths. These cases are eliminated from the system model by setting $i = 1, \ldots, N_{\text{rf}} - 1$.

2.4 | Model-based reconstruction

With above discrete system matrix, we use the conjugate gradient method to optimize the following cost function

$$\hat{\boldsymbol{f}} = \arg\min_{\boldsymbol{f}} \|\boldsymbol{s} - \boldsymbol{A}\boldsymbol{C}\boldsymbol{f}\|_2^2 + \beta R(\boldsymbol{f}), \tag{8}$$

where $\boldsymbol{s} = [\boldsymbol{s}_1; \ldots; \boldsymbol{s}_{N_{\text{rf}}}]$ is the vertically stacked signal, $\boldsymbol{A} = [(\boldsymbol{I} \otimes \tilde{\boldsymbol{A}}_1); \ldots; (\boldsymbol{I} \otimes \tilde{\boldsymbol{A}}_{N_{\text{rf}}})]$ is the stacked system matrix, and $R(\boldsymbol{f}) = \|\boldsymbol{D}f\|_2^2$ is a 3D roughness regularizer using quadratic

1st-order finite differences with 26 neighbors. We use CG-SENSE[23] with 30 iterations to optimize (8).

2.5 | k-space filtering and object basis spectrum

For gridding reconstruction of all protocols, a hard cut-off was used to truncate the k-space data with a k-space window at 50% (unless specified otherwise) to reduce the overlapping echo artifact.[15]

For model-based reconstruction, instead of filtering out the mixed signals, we model the echo-in and echo-out mixture using an object basis function whose spectrum $B(\boldsymbol{k})$ is Fermi shaped with a cutoff frequency around 90%. We use this 90% cutoff frequency because the magnitude of low-frequency components near the k-space origin is much larger than the magnitude of the high-frequency components; therefore when these two signals are superimposed, it is very difficult to recover the high-frequency components accurately. The Fermi filters must be applied to each subsystem matrix $\boldsymbol{A}_{il}$ individually before matrix combination because the echo-in and echo-out signals need to be filtered in "opposite" directions. One cannot apply two different filters to the data.

The exact shape of the spectrum of object basis function $B(\boldsymbol{k})$ depends on the pulse sequence parameters, such as the spatial resolution and number of spokes. Empirically, we chose a 90% cutoff frequency to reduce the mixture of center k-space signals and high-frequency signals coming from the echo-in and echo-out spokes, respectively. We then chose the transition band to reduce the ringing artifact that would be caused by a hard cutoff.

2.6 | Implementation and reproducible research

We used TOPPE[24] to program the looping-star pulse sequence on a GE UHP 3.0T scanner with a Nova Medical 32-channel Rx head coil.

We compared the proposed model-based reconstruction using echo-in and echo-out system matrices (MB-2 in figures below) to a simpler model-based reconstruction method that used a single echo-out system matrix, A_1 (MB-1 in figures below) and a gridding method that used a density compensation function and a gridding over-sampling factor of 2. Then we applied sensitivity map based complex coil combination to construct the final images. We tested the structural MRI protocol on three subjects and variants of the fMRI protocol on four subjects. Subjects gave informed consent under IRB approval from the University of Michigan.

For model-based reconstruction, we used the Matlab toolbox MIRT[28] to build the NUFFT-based system matrix and optimize the cost function.

3 | RESULTS

We demonstrated proposed model-based reconstruction approach on phantom and in vivo scans.

3.1 | Overlapping echo artifacts demonstration

Figure 2 illustrates the resultant effect for overlap of the echo-in and echo-out spokes in the gridding reconstruction. For k-space filter with a threshold of 0.5, there is little artifact, but resolution is lowered by roughly a factor or two in all three directions. For higher cutoffs, there is a trade-off between spatial resolution and artifact resulting from misassigned spatial frequency components.

3.2 | Phantom experiments

Figure 3 shows the reconstruction for structured phantom using a high-resolution looping-star protocol. We compare the standard GRE reconstruction results to looping-star reconstruction using gridding, model-based reconstruction without modeling overlapping signal (MB-1), and model-based method with overlapping signal modeling (MB-2). MB-2 significantly improved the spatial resolution by modeling the high-frequency components in sampled signals compared to the gridding method. Signal loss near the phantom-air edges is also recovered due to the spatial resolution improvement.

3.3 | In vivo experiments

The proposed method reduced the overlapping echo artifacts and improved the spatial-temporal resolution in both structural and functional MRI, compared to the conventional gridding method.

3.3.1 | Structural MRI

Figure 4 shows the reconstruction for a human brain scan in a representative subject using the high-resolution protocol (1.25-mm isotropic). The structural MRI results using hi-res protocol for the other two subjects are shown in Figure S1 to further support the increased spatial

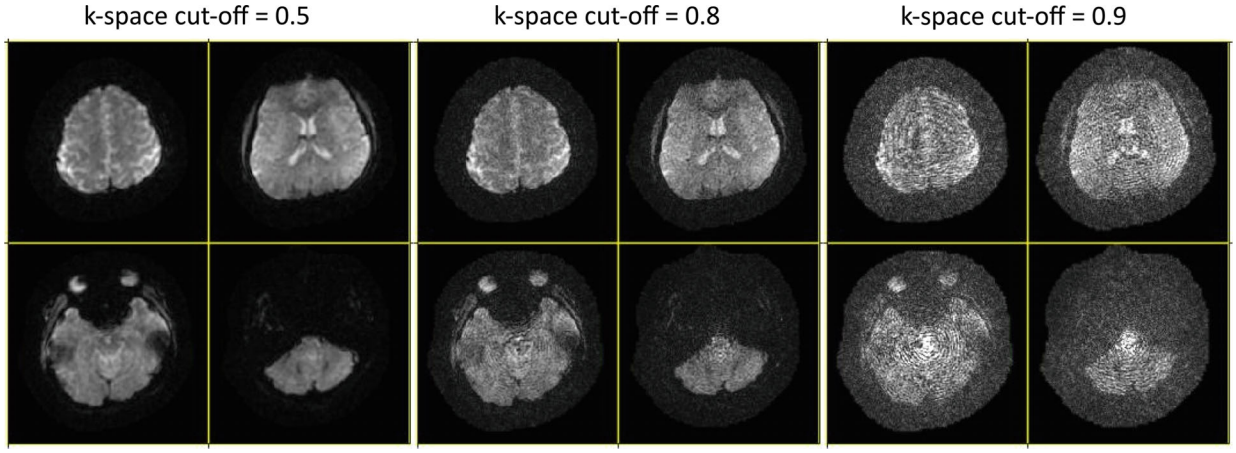

FIGURE 2 Overlapping echo artifact from the conventional gridding methods. As the k-space cut-off increases, the overlapping echo artifact can significantly degrade the image quality.

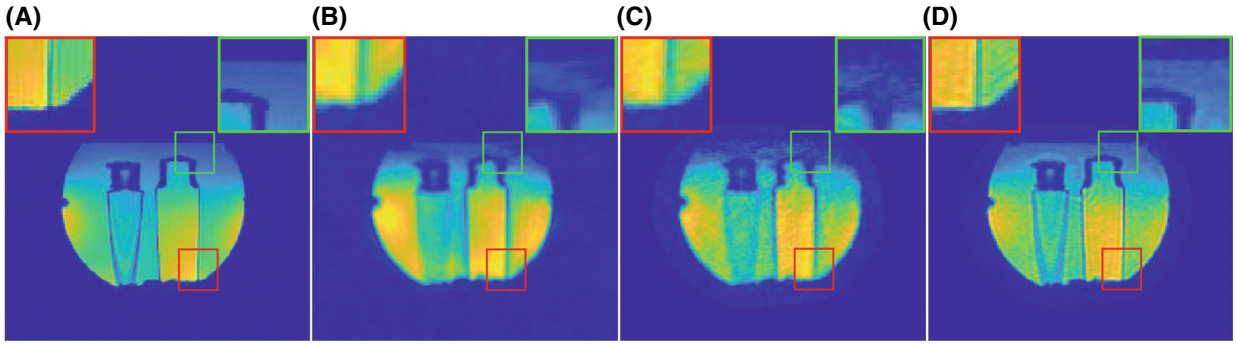

FIGURE 3 High-resolution looping-star reconstruction in phantom study. (A) standard T_2^*-weighted gradient echo (GRE) (scan time: 21 min); (B) Gridding reconstruction with density compensation function; (C) MB-1 without overlapping echo modeling; (D) MB-2 with overlapping echo modeling. For (B), (C), (D), all use the same k-space data with scan time of about 7 min. (D) shows similar spatial resolution (slightly reduced due to voxel indicator function and spherical acquisition pattern) to the standard GRE, and improved image quality compared to (B) and (C) in terms of sharper edges (red zoom-in box) and recovered signal loss (green zoom-in box). (A) Standard GRE; (B) gridding; (C) MB-1; (D) MB-2.

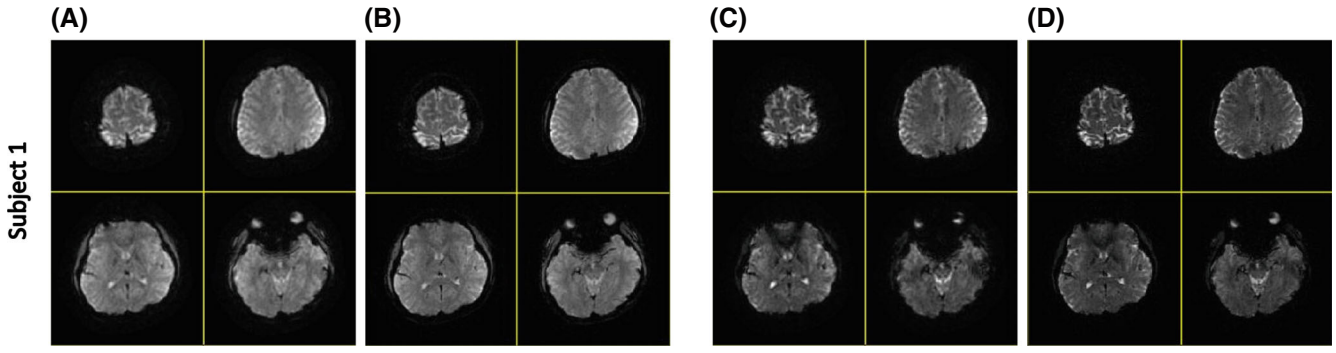

FIGURE 4 High-resolution looping star reconstruction for a representative subject. MB-2 provided improved spatial resolution and recovered signal loss, particularly in the inferior slices for echo 2, compared to gridding reconstruction. (A) Gridding (echo 1); (B) MB-1 (echo 2); (C) Gridding (echo 1); (D) MB-2 (echo 2).

resolution compared to the gridding method. For the gridding method, overlapping echo artifact was reduced by truncating the k-space, which also reduced the spatial resolution. The proposed MB-2 shows increased spatial resolution, reduced overlapping echo artifacts as well as improved image quality, compared to the gridding method.

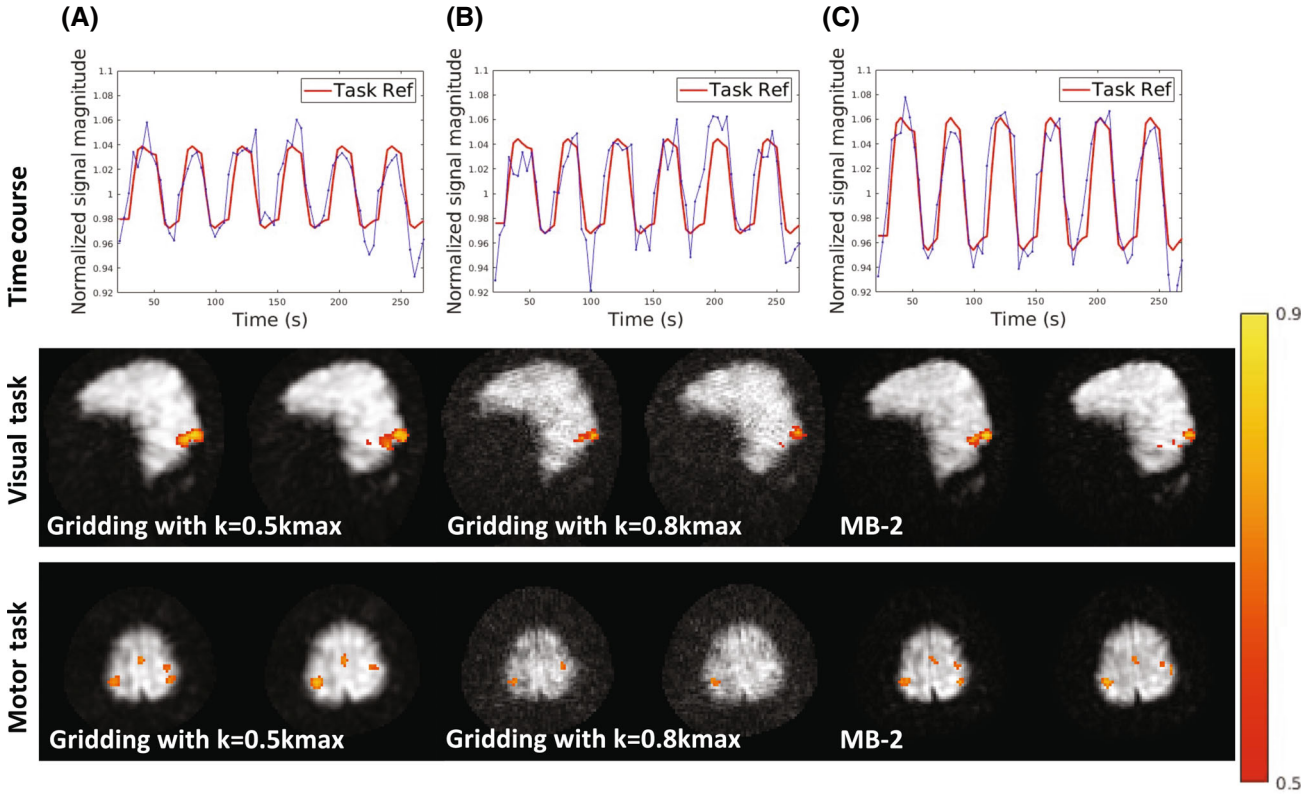

FIGURE 5 Functional MRI (fMRI) task result. First row: time course from the voxel with the highest correlation coefficient. With the improved spatial resolution, time course in MB-2 shows larger signal change due to the reduced partial volume effect. Second row: sagittal activation map for visual tasks (two consecutive slices). Although the undersampling artifact (20× undersampled) dominates the artifacts here, MB-2 reconstruction still shows slightly improved spatial resolution. With gridding method, activation map is smoothed and potentially showing false positives. Third row: Axial activation map for finger-tapping tasks (two consecutive slices). (A) Gridding with k = 0.5kmax; (B) gridding with k = 0.8kmax; (C) MB-2.

Besides the sharper images, the signal loss around frontal sinuses and ear canals is recovered due to the smaller voxel size. Due to almost halved spatial resolution, the gridding method has a 4× lower (better) undersampling rate than the MB-2 method. MB-2 method has higher undersampling rate and thus potentially more affected by the undersampling artifact even with Model-based reconstruction method. The reconstructions from other two subjects in Figure S1 support that MB-2 improves the spatial resolution by almost a factor of 2 and the circular ringing artifacts in the top right slices of subject 1 might have come from motion or other factors.

3.3.2 | Functional MRI

We demonstrated application of the proposed methods to fMRI by doing finger-tapping and visual fMRI tasks. In the fMRI study, healthy participants watched a flashing checkerboard for multiple cycles (20 s on and 20 s off), and were required to tap their fingers while the checkerboard was on. Figure 5 shows the activation map and time course for the finger-tapping test in a typical subject. The proposed MB-2 reconstruction method showed higher correlation and less noise on the activation map as compared to gridding method. Its time course also better matches the task reference and is less noisy.

4 | DISCUSSION

Compared to the standard GRE method, the biggest disadvantage of looping-star is the low SNR that limits its spatial and temporal resolution. By exploiting the high-frequency k-space information, the proposed method can resolve the overlapping echoes and use about twice as many signal samples for reconstruction, which also improves the SNR by a factor of nearly $\sqrt{2}$. However, since the high-frequency signal values are mixed with the low-frequency signals, which have a much larger magnitude, it is difficult to accurately estimate the highest-frequency components. To overcome this problem, we used a object basis spectrum based on a Fermi function that effectively leads to a slight

truncation of the high-frequency components (≈90%) at the end of the echo-in and echo-out spokes acquisition. This approach reduced the image distortion coming from the mis-estimation of the highest-frequency signals.

One other reconstruction method RF-cycling[14] leads to reduced temporal resolution. Another appraoch is coherence-resolved looping-star,[18] which removes most of the overlapping echo artifacts by pushing further in k-space before the next RF pulse is applied. This by done by increasing the gradient strength for a fixed number of RF pulses, thus increasing acquisition bandwidth, resulting in reduced SNR. Alternatively, the coherence-resolved approach can be implemented by reducing the number of RF pulses, which can maintain the SNR, but increases undersampling artifact by reducing the number of spokes. In all of these approaches, there is a loss of image quality, SNR or temporal resolution.

For the excitation process, considering the typical T1 value of the gray matter and 23 RF pulse of 3° flip angle and using small tip angle approximation, the Mz of the last RF pulse was indeed about 3.2% decreased compared to the first RF pulse for gray matter. Therefore, we neglected the impact of the Mz decrease in our signal model. RF-induced echo splitting and resulting higher-order echoes (spin-echoes, stimulated echoes, etc) are neglected, again, because of the low flip angles.[14] In addition, the higher-order echoes are also not re-phased in the gradient-echo module due to the continuously changing gradient fields.

We used 3D golden-angle-based sampling trajectories to achieve more uniformly distributed spokes. The performance of randomly rotated spokes highly depends on the random seed, so the image quality in each frame of fMRI studies would differ significantly if different sampling patterns for each frame were used. Accordingly, we repeated the a single 3D pattern for all fMRI temporal frames.

One potential issue with the proposed approach is whether poor conditioning could lead to noise amplification in the reconstruction. To examine this issue, we generated SD maps, estimated from 20 realizations of additive complex white Gaussian noise to the measured signal in the fMRI protocol. The SD maps in Figure S2 show that the model using echo-in and echo-out system matrices have nearly identical reconstruction noise relative to the model using echo-in system matrix only, indicating that using echo-in and echo-out system matrices does not worsen the conditioning or the noise amplification for the regularization parameters used in this work.

The traditional gridding method either suffers from low-spatial resolution and reduced signal change due to partial volume effects by truncating too much (truncation to $0.5k_{\max}$), or suffers from overlapping echo artifacts and more noise by truncating too little. The proposed MB-2 method resolves the overlapping echoes and showed improved spatial resolution (about 1.8× expected relative to the lower resolution gridding), larger signal change, and better activation compared to previous methods. The longer effective readouts for MB-2 can improve the SNR by a factor of $\sqrt{1.8}$, thus leading to a net SNR reduction of $\frac{\sqrt{1.8}}{1.8^3}$ compared to the gridding method, where the 1.8^3 comes from the reduced 3D voxel size. Still, the fMRI results did not appear to be limited by thermal noise. Quantifying spatial resolution and SNR will be part of our future work.

There are several other directions for improving image quality and SNR in future work. These include shaped RF pulses to reduced hard pulse shading across the field of view and variable flip angels schemes to maximize signal strength and uniformity. We will also consider approaches to optimize the sampling pattern using learning-based method to further reduce image artifacts and increase image qualities.[29] For multi-echo looping-star, learning-based networks can provide fast and accurate quantitative T_2^* mapping.[30] We will also further explore the possibility of using spatial-temporal reconstruction model in looping-star.[31]

5 | CONCLUSION

We proposed a novel model-based reconstruction method to resolve the overlapping echo challenge in looping-star pulse sequences. We also used a 3D golden-angle based sampling pattern and mid-resolution fMRI protocol to further improve the image quality in the fMRI studies. By exploiting the high-frequency k-space information, the proposed approach was able to recover high-resolution images and reduce the artifacts compared to previous methods, while preserving the temporal resolution in fMRI.

ACKNOWLEDGMENTS

The authors think Dr. Jon-Fredrik Nielsen for helpful discussions.

DATA AVAILABILITY STATEMENT

The in-house looping-star implementation and reconstruction code will be available at https://github.com/haoweix/MBLS after paper acceptance.

ORCID

Haowei Xiang https://orcid.org/0000-0001-7598-9480
Jeffrey A. Fessler https://orcid.org/0000-0001-9998-3315
Douglas C. Noll https://orcid.org/0000-0002-0983-3805

TWITTER

Haowei Xiang HaoweiXiang

REFERENCES

1. Quirk ME, Letendre AJ, Ciottone RA, Lingley JF. Anxiety in patients undergoing MR imaging. *Radiology*. 1989;170:463-466.
2. Cho ZH, Chung SC, Lim DW, Wong EK. Effects of the acoustic noise of the gradient systems on fMRI: a study on auditory, motor, and visual cortices. *Magn Reson Med*. 1998;39:331-335.
3. Bandettini PA, Jesmanowicz A, Van Kylen J, Birn RM, Hyde JS. Functional MRI of brain activation induced by scanner acoustic noise. *Magn Reson Med*. 1998;39:410-416.
4. Yakunina N, Kang EK, Kim TS, Min JH, Kim SS, Nam EC. Effects of scanner acoustic noise on intrinsic brain activity during auditory stimulation. *Neuroradiology*. 2015;57:1063-1073.
5. Tomasi D, Caparelli EC, Chang L, Ernst T. fMRI-acoustic noise alters brain activation during working memory tasks. *Neuroimage*. 2005;27:377-386.
6. Talavage TM, Edmister WB, Ledden PJ, Weisskoff RM. Quantitative assessment of auditory cortex responses induced by imager acoustic noise. *Hum Brain Mapp*. 1999;7:79-88.
7. Peelle JE. Methodological challenges and solutions in auditory functional magnetic resonance imaging. *Front Neurosci*. 2014;8:253.
8. Moelker A, Pattynama PM. Acoustic noise concerns in functional magnetic resonance imaging. *Hum Brain Mapp*. 2003;20:123-141.
9. Peelle JE. Listening effort: how the cognitive consequences of acoustic challenge are reflected in brain and behavior. *Ear Hear*. 2018;39:204-214.
10. McJury MJ. Acoustic noise and magnetic resonance imaging: a narrative/descriptive review. *J Magn Reson Imaging*. 2022;55:337-346.
11. Edelstein WA, Kidane TK, Taracila V, et al. Active-passive gradient shielding for MRI acoustic noise reduction. *Magn Reson Med*. 2005;53:1013-1017.
12. Hennel F, Girard F, Loenneker T. "Silent" MRI with soft gradient pulses. *Magn Reson Med*. 1999;42:6-10.
13. Weiger M, Pruessmann KP, Hennel F. MRI with zero echo time: hard versus sweep pulse excitation. *Magn Reson Med*. 2011;66:379-389.
14. Wiesinger F, Menini A, Solana AB. Looping star. *Magn Reson Med*. 2019;81:57-68.
15. Dionisio-Parra B, Wiesinger F, Sämann PG, Czisch M, Solana AB. Looping star fMRI in cognitive tasks and resting state. *J Magn Reson Imaging*. 2020;52:739-751.
16. Matsuo-Hagiyama C, Watanabe Y, Tanaka H, et al. Comparison of silent and conventional MR imaging for the evaluation of myelination in children. *Magn Reson Med Sci*. 2017;16:209-216.
17. Shrestha M, Lee HS, Nöth U, Deichmann R. A novel sequence to improve auditory functional MRI with variable silent delays. *Magn Reson Med*. 2021;85:883-896.
18. Damestani N, Lythgoe DJ, Solana AB, et al. Coherence-resolved looping star – improvements for silent multi-gradient echo structural and functional neuroimaging. Paper presented at: Proceedings of the 30th Annual Meeting of the ISMRM 2021. #2667
19. Fessler JA. Model-based image reconstruction for MRI. *IEEE Signal Process Mag*. 2010;27:81-89.
20. Xiang H, Fessler JA, Noll DC. Model-based image reconstruction in looping-star MRI. Paper presented at: Proceedings of the 31th Annual Meeting of the ISMRM. 2022; London, UK. Abstract #2346.
21. Fyrdahl A, Holst K, Caidahl K, Ugander M, Sigfridsson A. Generalization of three-dimensional golden-angle radial acquisition to reduce eddy current artifacts in bSSFP CMR imaging. *Magn Reson Mater Phys Biol Med*. 2021;34:109-118.
22. Leynes AP, Damestani NL, Lythgoe DJ, et al. Extreme looping star: quiet fMRI at high spatiotemporal resolution. Paper presented at: Proceedings of the 30th Annual Meeting of the ISMRM 2021. Abstract 0458.
23. Pruessmann KP, Weiger M, Börnert P, Boesiger P. Advances in sensitivity encoding with arbitrary k-space trajectories. *Magn Reson Med*. 2001;46:638-651.
24. Nielsen JF, Noll DC. TOPPE: a framework for rapid prototyping of MR pulse sequences. *Magn Reson Med*. 2018;79:3128-3134.
25. Hennig J, Hodapp M. Burst imaging. *Magn Reson Mater Phys Biol Med*. 1993;1:39-48.
26. Chan RW, Ramsay EA, Cunningham CH, Plewes DB. Temporal stability of adaptive 3D radial MRI using multidimensional golden means. *Magn Reson Med*. 2009;61:354-363.
27. Sutton BP, Noll DC, Fessler JA. Fast, iterative image reconstruction for MRI in the presence of field inhomogeneities. *IEEE Trans Med Imaging*. 2003;22:178-188.
28. Fessler JA. Michigan image reconstruction toolbox (MIRT). Accessed September 5, 2019. https://github.com/JeffFessler/mirt
29. Wang G, Nielsen J-F, Fessler JA, Noll DC. Stochastic optimization of 3D non-Cartesian sampling trajectory (SNOPY). *Mag Reson Med*. 2023;90:417-431.
30. Xu X, Kothapalli SV, Liu J, et al. Learning-based motion artifact removal networks for quantitative R2* mapping. *Magn Reson Med*. 2022;88:106-119.
31. Xiang H, Fessler JA, Noll DC. Spatial-temporal reconstructionusing UNFOLD in looping-star silent fMRI. Proceedings of the 32th Annual Meeting of the ISMRM. Vol 2534. 2023.

SUPPORTING INFORMATION

Additional supporting information may be found in the online version of the article at the publisher's website.

Section S.1 Object basis function

Section S.2 Spatial resolution

Figure S1. High-resolution looping star reconstruction for two additional subjects. The proposed MB-2 approach provided improved spatial resolution and recovered signal loss in multiple areas compared to gridding reconstruction.

Figure S2. Reconstruction and variance maps. (A) shows the high-resolution reconstruction for references. (B) and (C) are the SD maps using echo-out system matrix only and both echo-in and echo-out system matrices respectively. (D) and (E) are corresponding histogram of these four slices. We generated SD maps, estimated from 20 realizationsof additive complex white Gaussian noise to the measured signal in the fMRI protocol. The model using echo-in and echo-out system matrices have nearly identical reconstruction noise relative to the model using echo-in system matrix only, indicating that using echo-in and echo-out system matrices does not worsen the conditioning or the

noise amplification for the regularization parameters used in this work.

Figure S3. FWHM of PSF over iterations and MB-2 reconstruction at different iteration. (A) shows the FWHM of PSF over CG-iterations. The FWHM of PSF is computed by reconstructing the k-space data of a Kronecker impulse function. The PSF gradually converged after 50 iterations. (B) shows the MB-2 reconstructions of the same subject at iteration 30 and 100 with zero initialization. Though the PSF still decreases after 30 iterations, the change in the reconstructed images is nonvisible, so for most of the results shown in the paper, we stopped at 30 iteration to save compute time. The FWHM of PSF using gridding method is measured to be 3.59 pixels for comparison. (C) compares the PSF from the center slice of the subject. The curve shows the radial FWHM of all direction and the overall FWHM is the averaged value.

How to cite this article: Xiang H, Fessler JA, Noll DC. Model-based reconstruction for looping-star MRI. *Magn Reson Med*. 2024;91:2104-2113. doi: 10.1002/mrm.29927

Model-based reconstruction for looping-star MRI
Supporting information

H. Xiang, J. A. Fessler, D. C. Noll

October 28, 2023

S.1 Object basis function

The Fermi filters must be applied to each sub-system matrix individually before matrix combination because the echo-in and echo-out signals need to be filtered in 'opposite' directions. One cannot apply two different filters directly to the data.

The exact shape of the spectrum of object basis function $B(k)$ depends on the pulse sequence parameters, such as the spatial resolution and number of spokes. Empirically, we chose a 90% cutoff frequency to reduce the mixture of center k-space signals and high-frequency signals coming from the echo-in and echo-out spokes respectively. We then chose the transition band to reduce the ringing artifact that would be caused by a hard cutoff.

S.2 Spatial resolution

The actual spatial resolution in reconstructed images is related to the regularization parameters when using roughness and many other regularizers. Therefore, regularization parameters need to be chosen carefully here as one of the main goals for using model-based reconstruction is to improve spatial resolution.

Here we empirically chose the regularization factors such that undersampling artifact can be mitigated while preserving most of the spatial resolution. We report the full width at half maximum (FWHM) values and corresponding regularization factors here to help understand the relationship between spatial resolution and regularization factors. Fig. S3 shows the FWHM of the point spread function (PSF) over iterations and the reconstructed images at 30 and 100 iterations. The FWHM of MB-2 method is about 2.5 pixels at 50 iteration and the FWHM of gridding method is about 3.6 pixels.

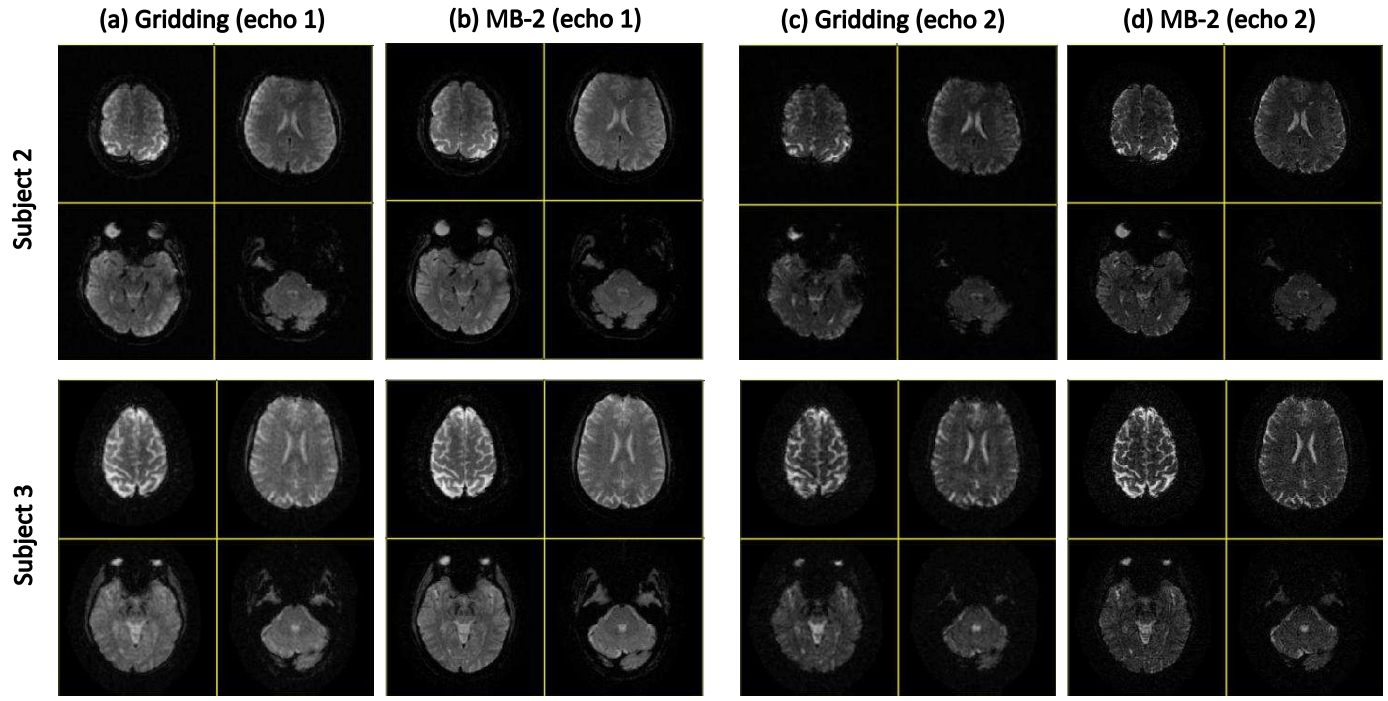

Figure S1: Hi-resolution looping star reconstruction for two additional subjects. The proposed MB-2 approach provided improved spatial resolution and recovered signal loss in multiple areas compared to gridding reconstruction.

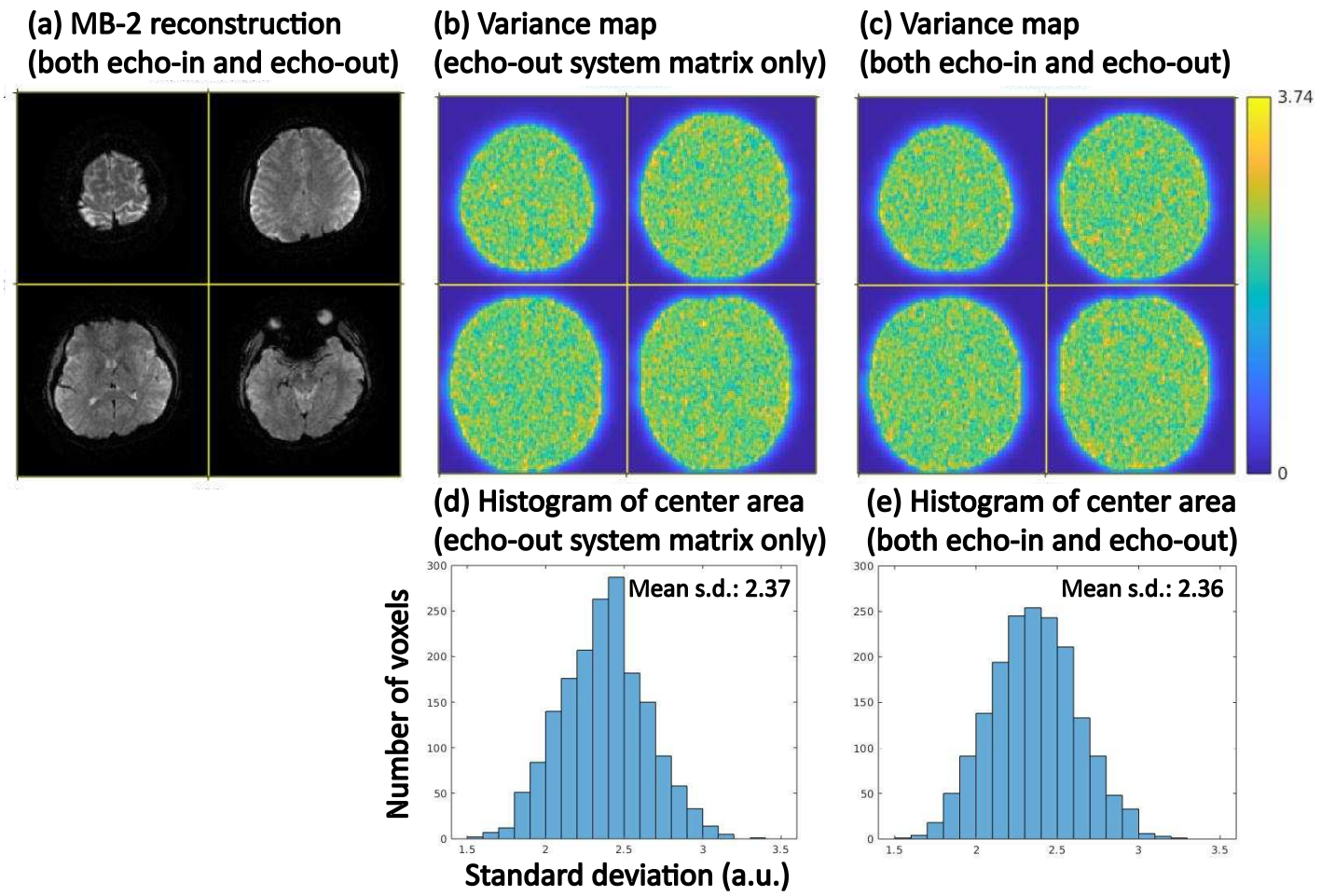

Figure S2: Reconstruction and variance maps. (a) shows the hi-resolution reconstruction for references. (b) and (c) are the standard deviation maps using echo-out system matrix only and both echo-in and echo-out system matrices respectively. (d) and (e) are corresponding histogram of these 4 slices. We generated standard deviation maps, estimated from 20 realizations of additive complex white Gaussian noise to the measured signal in the fMRI protocol. The model using echo-in and echo-out system matrices have nearly identical reconstruction noise relative to the model using echo-in system matrix only, indicating that using echo-in and echo-out system matrices does not worsen the conditioning or the noise amplification for the regularization parameters used in this work.

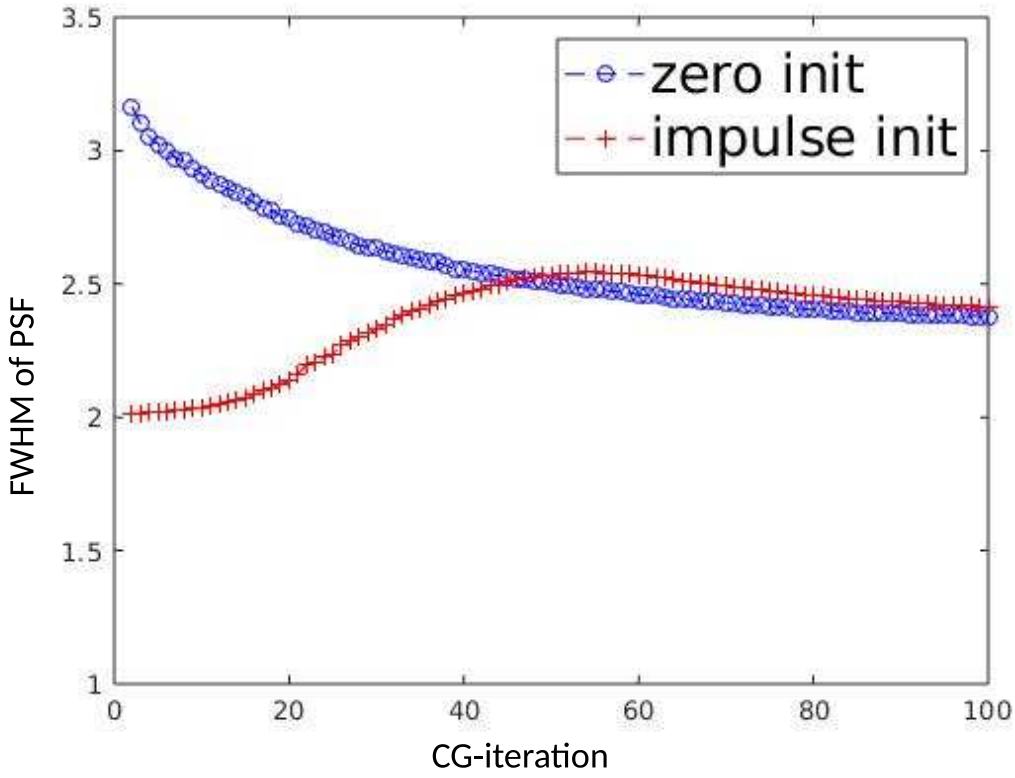

(a) FWHM of PSF over iterations

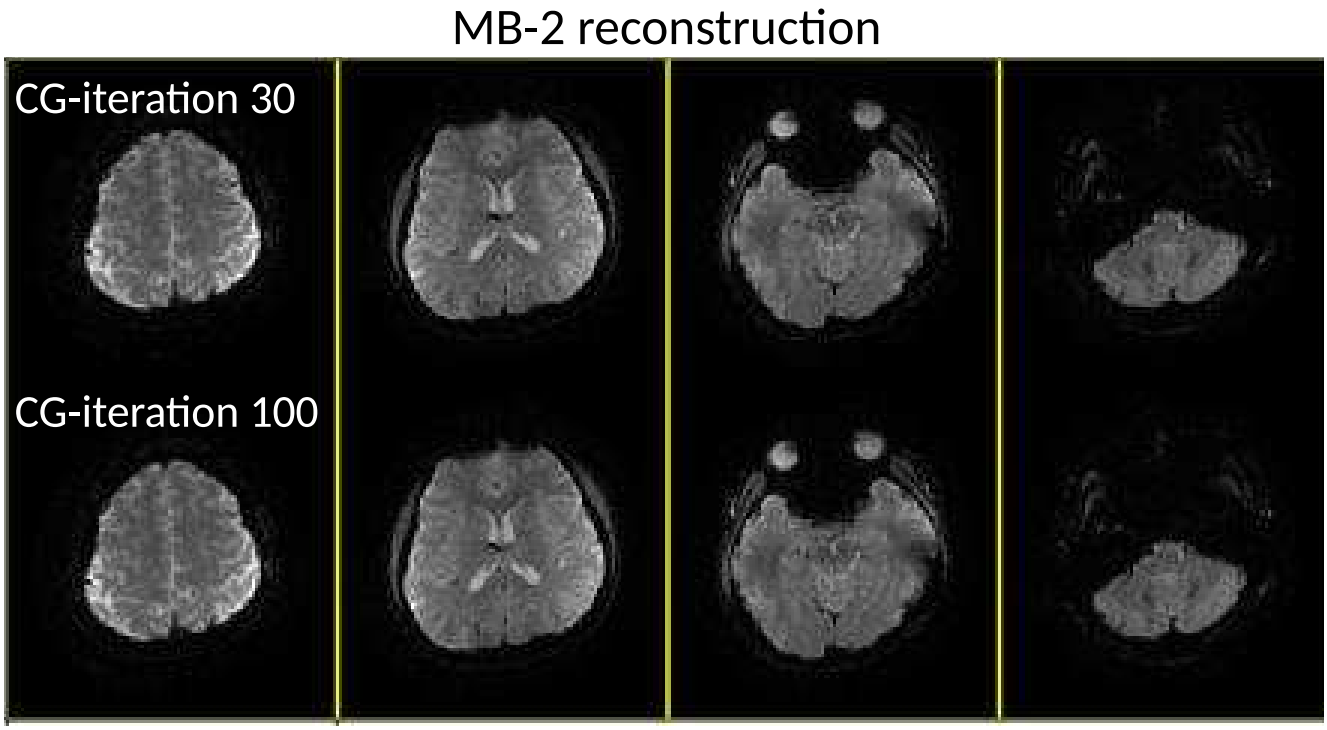

(b) MB-2 reconstruction at different iteration

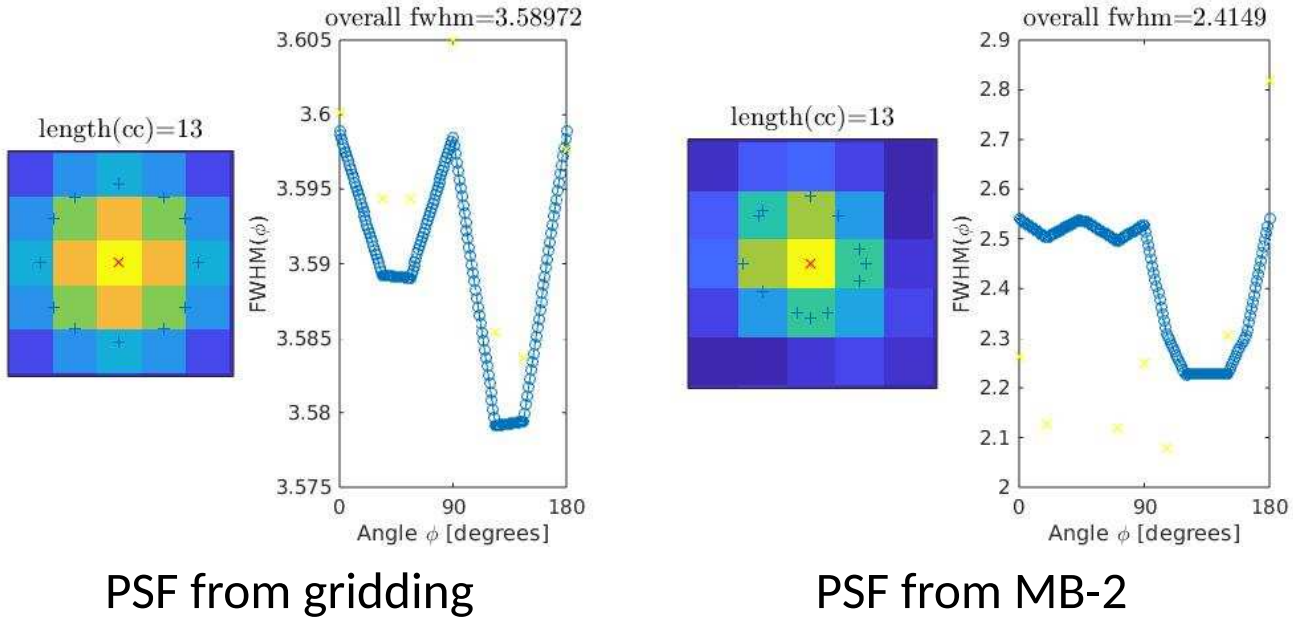

(c) PSF comparison between gridding and MB-2

Figure S3: FWHM of PSF over iterations and MB-2 reconstruction at different iteration. (a) shows the FWHM of PSF over CG-iterations. The FWHM of PSF is computed by reconstructing the k-space data of a Kronecker impulse function. The PSF gradually converged after 50 iterations. (b) shows the MB-2 reconstructions of the same subject at iteration 30 and 100 with zero initialization. Though the PSF still decreases after 30 iterations, the change in the reconstructed images is non-visible, so for most of the results shown in the paper, we stopped at 30 iteration to save compute time. The FWHM of PSF using gridding method is measured to be 3.59 pixels for comparison. (c) compares the PSF from the center slice of the subject. The curve shows the radial FWHM of all direction and the overall FWHM is the averaged value.